ROYAL SOCIETY OF CHEMISTRY

PAPER

Check for updates

A wearable DC tribovoltaic power textile woven by P/N-type organic semiconductor fibers†

Beibei Fan,[ac] Guoxu Liu,[ab] Yiming Dai,[ac] Zefang Dong,[ab] Ruifei Luan,[ab] Likun Gong, [ID][ab] Zhi Zhang, [ID][ab] Zhong Lin Wang[abde] and Chi Zhang [ID] *[abc]

High-performance direct current (DC) textile power supply is an urgent demand for wearable electronics. Herein, we present a wearable DC power textile woven by P/N-type organic semiconductor fibers based on the tribovoltaic effect. The hydrophobic P-type semiconductor PEDOT: PF and N-type semiconductor poly(benzodifurandione) are woven into a spiral fiber (SF). By serial/parallel combination, the SFs are woven into a wearable DC power textile (WDP). The WDPs can provide a DC output of 40 V, 2.2 mA, and power density can reach 1.05 W m^{-2}, approximately 75 times higher than that of previous textile triboelectric nanogenerators. With excellent human morphology adaptability and long-term stability of 72 000 cycles, electronic devices such as commercial lithium-ion batteries, mobile phones and ink electronic screens can be directly powered by the WDPs. The high-performance WDP provides a promising strategy for the practical application of the tribovoltaic effect in the field of textile power supplies and smart wearable electronics.

Broader context

As society moves into the age of the Internet of Things, artificial intelligence, and big data, wearable movable smart gadgets with smaller sizes and more complex functions are growing in popularity. It is vital to develop eco-friendly, light, durable, and adaptable flexible power sources. Fiber textile materials are commonly found in human life, and they can effectively adapt to complex deformations caused by body movement; they are ideal carriers for collecting kinetic energy from the human body. The tribovoltaic effect is a phenomenon of the generation of direct voltage and current by mechanical friction at the semiconductor interface; hence, we present a wearable DC power textile woven by P/N-type organic semiconductor fibers based on the tribovoltaic effect. The WDPs can provide a DC output of 40 V, 2.2 mA, and their power density can reach 1.05 W m^{-2}; with excellent human morphology adaptability and long-term stability of 72 000 cycles, the WDPs can directly power electronic devices such as commercial lithium-ion batteries, mobile phones and ink electronic screens. The high-performance WDP provides a promising strategy for the practical application of the tribovoltaic effect in the field of textile power supplies and smart wearable electronics.

Introduction

As society moves into the age of the Internet of Things, artificial intelligence, and big data, wearable movable smart gadgets

[a] CAS Center for Excellence in Nanoscience, Beijing Key Laboratory of Micro-nano Energy and Sensor, Beijing Institute of Nanoenergy and Nanosystems, Chinese Academy of Sciences, Beijing 101400, China. E-mail: czhang@binn.cas.cn

[b] School of Nanoscience and Technology, University of Chinese Academy of Sciences, Beijing 100049, China

[c] Center on Nanoenergy Research, School of Physical Science and Technology, Guangxi University, Nanning, China

[d] Georgia Institute of Technology, Atlanta, GA, USA

[e] Guangzhou Institute of Blue Energy, Knowledge City, Huangpu District, Guangzhou 510555, China

† Electronic supplementary information (ESI) available. See DOI: https://doi.org/10.1039/d4ee02662d

with smaller sizes and more complex functions are growing in popularity.[1–3] Theoretically, an endless, easily accessible, and eco-friendly power supply system is required to power these low-power wearable electronic devices.[4–6] However, rechargeable capacitors/batteries currently fall short of meeting future sustainable and environmentally acceptable energy needs due to inherent issues such as frequent charging requirements, waste disposal difficulties and safety risks.[7–9] Hence, it is vital to develop eco-friendly, light, durable, and adaptable flexible power sources. Fiber textile materials are commonly used in human life, and they can effectively adapt to complex deformations caused by body movements. They are an ideal carrier for collecting kinetic energy from the human body.[10–14] Developing smart textiles that generate electrical energy from mechanical movements is an effective approach to the upcoming era of wearable electronics. Scientists have recently developed a

This journal is © The Royal Society of Chemistry 2024

Energy Environ. Sci., 2024, **17**, 8621–8632 | **8621**

variety of green and sustainable textile power sources based on piezoelectric, triboelectric, thermoelectric, photovoltaic, and electrochemical effects.[11,15–20] Among them, the biocompatible and flexible fiber-based triboelectric nanogenerators (TENGs), which can convert biomechanical kinetic energy into electrical energy, have attracted particular attention from scientists.[21–29] The TENG is based on contact electrification and electrostatic induction; however, it does not match wearable smart electronics due to their high voltage, high impedance, low current density, and AC output characteristics.[4,30–32] In addition, a humid environment can cause surface charge dissipation of most fiber materials, affecting the contact electrification effect and further limiting the application of the fiber-based TENG.[6,10,14,30] The development of textile power supplies that possess characteristics such as low impedance, high DC current density and humidity resistance continues to present a noteworthy challenge.[14,33–35]

The tribovoltaic effect is a phenomenon of the generation of direct voltage and current by mechanical friction at the semiconductor interface, in which the friction forms new chemical bonds to release energy called "bindington" and excite the electron–hole pairs at the semiconductor interface, thus resulting in a DC by the action of a built-in electric field or interfacial electric field.[36–41] The tribovoltaic nanogenerator (TVNG) is a very promising technology for the direct conversion of mechanical energy into DC electricity in smart wearable electronics. Recently, scientists have developed various power textiles based on the tribovoltaic effect. Wang and Liu et al. reported a planar friction structure of Al/organic-semiconductor PEDOT:PSS fabrics, where a dynamic Schottky contact interface can generate DC electricity when the Al slides continuously on the fabric.[42,43] Due to its excellent conductivity and hydrophobicity, polypyrrole (PPy) is one of the best materials in the field of flexible electronics. Shao et al. slid (or pressed) aluminum (or gold) on PPy conductive textiles to generate direct current, and its current density has made a breakthrough.[44–46] Dong et al. developed an all fabric-based TVNG with a plane/plane friction mode, and its output characteristics were examined under various interfacial friction scenarios.[47] However, most fiber-based TVNGs are in the plane/plane friction mode, which not only occupies a large space and leads to the loss of garment aesthetics but also does not match the human body morphology movement, resulting in low energy harvesting efficiency. In addition, the lower power function difference between semiconductor interfaces causes the output voltage of TVNGs to be about 0.1–1.0 V. The fiber-based TVNGs in the plane/plane friction mode would seriously undermine the portability of wearable devices. Therefore, developing textile power supplies that are comfortable to wear, form-fitting, highly moisture-resistant, mechanically robust, high voltage, high DC and low impedance remains a great challenge.[4,10,13,14]

In this work, we present an organic semiconductor fiber-based wearable tribovoltaic DC power textile. The poly(3,4-ethylenedioxythiophene):perfluorinated sulfonic acid (PEDOT:PF) and poly(benzodifurandione) (PBFD) are woven into a spiral fiber (SF). By serial/parallel combination, the SFs are woven into a wearable DC power textile (WDP). The influence of diameter, mechanical stress, movement pattern (tensile state and compression states) and series/parallel parameters on the electrical output of the WDPs were systematically investigated. The open-circuit voltage (V_{oc}) and short-circuit current (I_{sc}) of WDP are 40 V and 2.2 mA, respectively, and its power density can reach 1.05 W m^{-2}, which is approximately 75 times higher than that of previous textile TENGs and TVNGs. The performance of WDP does not degrade after 72 000 cycles, and it still maintains 80% output performance in a humid environment of 90%. The WDPs still maintain 70% output performance after being washed 15 times and 117 days with no loss of performance. The WDPs achieve a 3.1-fold improvement in durability and a 11.5-fold reduction in internal resistance compared to previous textile TENGs and TVNGs, which can charge a 10 mF commercial capacitor to 5 V in 67 s and a commercial lithium-ion battery to 3 V in 55 min. The WDPs are well matched to human morphological motions and can directly power smart devices such as mobile phones, sports wristbands and colourful electric lights when the body is in motion without power management. The high-performance WDPs demonstrated in this work provide a promising strategy for the practical application of the tribovoltaic effect in the field of textile power supplies and smart wearable electronics.

Results and discussion

Material design and working mechanism

In this work, the hydrophobic P-type organic semiconductor solution (PEDOT:PF, Fig. S1A and B, ESI†) and N-type organic semiconductor solution (PBFD, Fig. S1C and D, ESI†) were prepared, and two functional fibers with P-type and N-type semiconductor properties were prepared by interfacial adsorption and impregnation methods. To ensure a tight friction interface between the P-type and N-type semiconductor fibers, we employed the spiral winding method, resulting in a three-dimensional spiral structure. Fig. 1A shows the fabrication process of two semiconductor fibers. Firstly, the plasma treatment of the cotton fibers (CFs) was done to enhance the surface activity of CFs. For the preparation of PEDOT:PF@Ti$_3$C$_2$@CFs semiconductor fibers, due to the excellent conductivity and hydrophilicity, Ti$_3$C$_2$ offers the possibility of fabricating advanced flexible electronic materials. For making PEDOT:PF completely adsorbed on the CF surface, PEDOT:PF@Ti$_3$C$_2$ was first prepared by the electrostatic self-assembly method. Firstly, the CFs were immersed in cetyltrimethylammonium bromide (CTAB) solution and sonicated for 1 h. Next, the CFs-CTAB were immersed in a multilayer Ti$_3$C$_2$ solution (Fig. S1E and F, ESI†) for 1 h to facilitate interfacial electrostatic self-assembly. Finally, the fibers were dried under vacuum at 60 °C for 12 h to obtain the Ti$_3$C$_2$@CFs fibers (Fig. S2A, ESI†). The polymerization process for PEDOT:PF is described briefly in Methods, wherein we utilized perfluorosulfonic acid (PF) ionomers as counterions in the alcohol phase to prepare semiconductor solutions.[48] Following that, the Ti$_3$C$_2$@CFs fibers were directly immersed into the PEDOT:PF solution, continuously stirred for

8622 | Energy Environ. Sci., 2024, **17**, 8621–8632

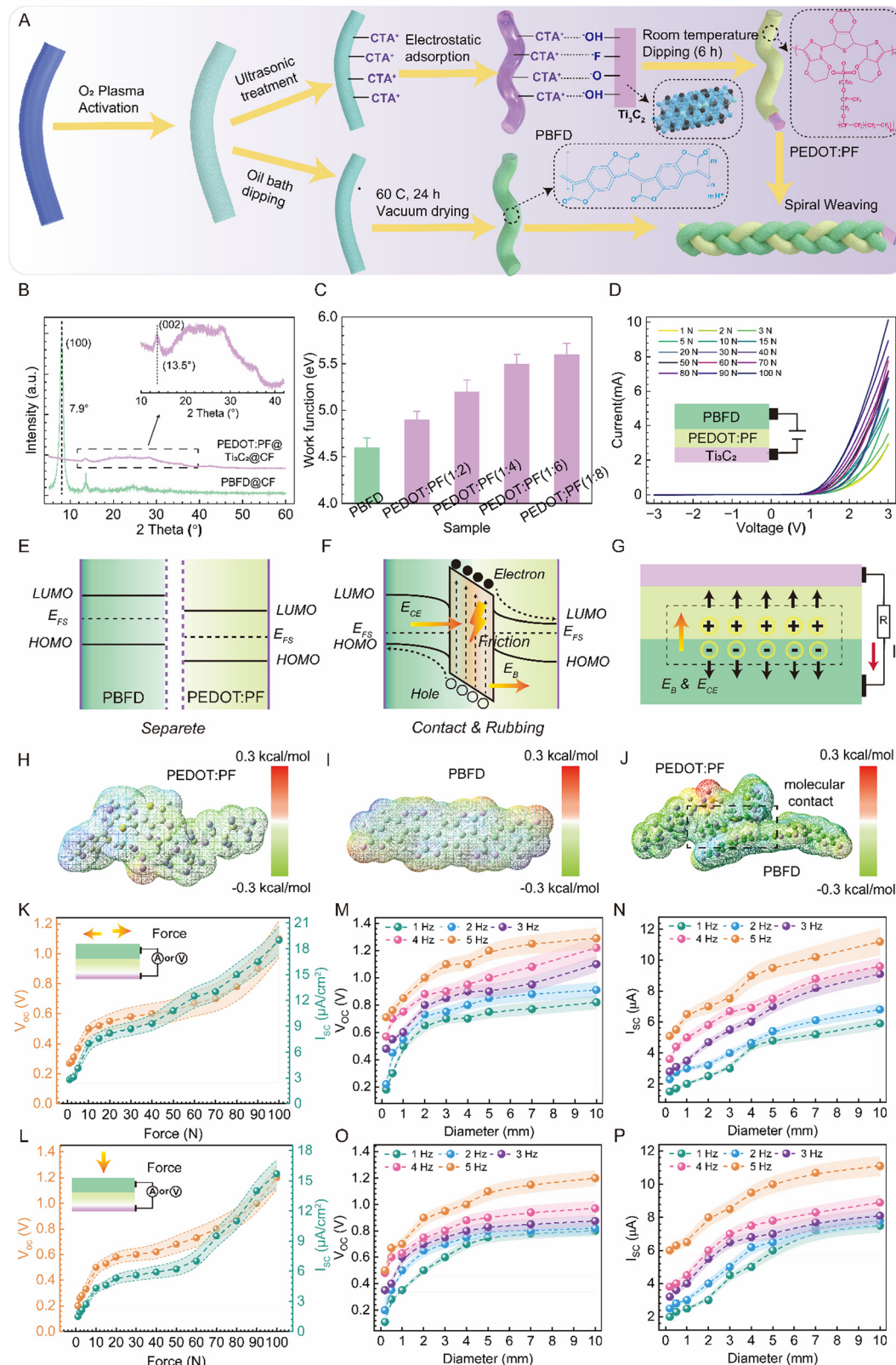This journal is © The Royal Society of Chemistry 2024

Fig. 1 Material design and working mechanism. (A) Schematic illustration of PEDOT:PF@Ti$_3$C$_2$@CFs, PBFD@CFs and SFs. (B) XRD patterns of PEDOT:PF@Ti$_3$C$_2$@CFs and PBFD@CFs. (C) Work function of PEDOT:PF@Ti$_3$C$_2$@CFs and PBFD@CFs. (D) I–V characteristic of the PEDOT:PF/PBFD heterojunction. (E)–(G) Energy band diagram from the separate state to the rubbing state, changes in energy levels and charge distribution. (H)–(J) Differential charge distribution based on molecular dynamics simulations. (K) and (L) V_{oc} and I_{sc} of sliding mode and compression mode generated by the PEDOT:PF/PBFD interface. (M)–(P) V_{oc} and I_{sc} of SFs under different diameters and frequencies.

This journal is © The Royal Society of Chemistry 2024

Energy Environ. Sci., 2024, **17**, 8621–8632 | **8623**

2 h, and finally vacuum-dried at 60 °C for 12 h to achieve PEDOT:PF@Ti$_3$C$_2$@CFs semiconductor fibers (Fig. S2B, ESI†). For the preparation of PBFD@CFs semiconductor fibers, the CFs fibers were stirred in the PBFD solution at 50 °C for 6 h, followed by vacuum drying at 50 °C for 24 h. By doing so, PBFD@CFs semiconductor fibers were obtained (Fig. S2C, ESI†). To complete the process, both the PEDOT:PF@Ti$_3$C$_2$@CFs semiconductor fibers and PBFD@CFs semiconductor fibers were woven into a three-dimensional single helical structure using the helical winding method (Fig. S3, ESI†).[49–51] In Fig. 1B, the X-ray diffraction (XRD) pattern displays characteristic peaks that confirm the successful synthesis of both PEDOT:PF@Ti$_3$C$_2$@CFs semiconductor fibers and PBFD@CFs semiconductor fibers. In the case of PEDOT:PF@Ti$_3$C$_2$@CFs semiconductor fibers, the sharp (002) peak at 13.5° corresponds to the multilayer Ti$_3$C$_2$, whereas the wide amorphous peak observed in the range of 20–30° represents the composite of CFs and PEDOT:PF. On the other hand, the peak (100) at 7.9° in the XRD pattern of PBFD@CFs semiconductor fibers indicates the characteristic peak of PBFD.[52] These XRD results further support the successful synthesis of the desired semiconductor fibers.

The work function of semiconductor heterojunction interface materials significantly influences their electrical properties. Consequently, the work functions of PBFD and PEDOT:PF with different molar ratios are investigated. In Fig. 1C, the work function of the N-type PBFD is 4.6 eV. In contrast, the work function of the P-type PEDOT:PF increases as the ratio of anti-ionic PF rises. When the PEDOT to PF ratio is 1:2, the work function reaches 4.9 eV, while a ratio of 1:8 results in a work function of 5.7 eV (Fig. S4, ESI†). A higher work function in PEDOT:PF facilitates the formation of upward band bending at the interface when in contact with the polymer donor, enhancing efficient hole collection. Moreover, a larger work function difference at the interface contributes to an improved interface barrier and increased V_{oc}.[34,41,43] Fig. 1D illustrates the I–V characteristics of PBFD/PEDOT:PF (1:8) at the heterogeneous interface under mechanical pressure ranging from 1 to 100 N. The I–V curves exhibit a typical Schottky contact, introducing a strong internal electric field at the interface, which is a key factor in the manufacture of high-performance TVNGs.

The working mechanism of TVNG with PBFD/PEDOT:PF Schottky contact is based on the tribovoltaic effect, as shown in Fig. 1E and F. In the sliding mode, the work function of PBFD is lower than that of PEDOT:PF before the contact. When PBFD and PEDOT:PF come into contact, electrons transfer from PBFD to PEDOT:PF, aligning their Fermi energy levels. This generates a built-in electric field (E_b) at the PBFD/PEDOT:PF interface, forming a space charge layer. Consequently, the energy levels of PEDOT:PF (the conduction band) bend downwards at the interface. During the sliding process, the mechanical energy produced by friction separates the electron–hole pairs at the interface. Electrons are excited into the conduction band, while a large number of holes remain in the valence band. As depicted in Fig. 1G, under the influence of E_b, electrons flow from PEDOT:PF to PBFD, and holes flow in the opposite direction, resulting in a continuous DC. In addition,

previous studies have shown that the induced electric field (E_{CE}) generated by contact electrification can also affect the movement of heterojunction charge carriers.[43,47,53] To obtain the direction of the E_{CE}, the change in surface potential of PEDOT: PF during the friction process between PEDOT: PF and PBFD was investigated, as shown in Fig. S5 (ESI†). The surface of PEDOT: PF was negatively charged, indicating the presence of contact electrification. The E_{CE} was directed from PBFD to PEDOT: PF. The electric fields E_b and E_{CE} are in the same direction, and the carriers move in one direction in the superposition of E_b and E_{CE}. The charge distributions and electrostatic potentials of the two semiconductor molecules from the separation state to the contact state were further simulated by molecular dynamics as in Fig. 1H–J and Fig. S6 (ESI†). As shown in Fig. 1H and I, when the two semiconductors are in an independent state, in the PEDOT:PF molecular system, the –CF$_3$ group exhibits the strongest electronegativity and the C–C ring structure exhibits the strongest positive electronegativity, and in the PBFD molecular system, the consecutive benzene ring structure exhibits positive electronegativity and the C=O group exhibits electronegativity. When the two molecules come into contact, –CF$_3$ PEDOT:PF exhibits the greatest negative potential, and the benzene ring structure in PBFD exhibits the greatest negative potential, showing that PBFD tends to be positively charged and PEDOT:PF tends to be negatively charged (Fig. 1J).

Some work has shown that in the compression state, compression force can cause a decrease in the Schottky barrier height at the interface and that the decrease in barrier height breaks the equilibrium and causes electrons to shift at the interface, a situation that generally requires a higher pressure.[44–46] Some previous studies have suggested that the "mechanochemical" effect arising from contact charging is likely to be the cause.[54] Specifically, when atoms at the interface of the two materials come close together, atom-atom interactions or new bonds form through overlapping electron clouds, as illustrated in the Fig. S7 (ESI†) model. In this process, the continuous input of frictional energy will lead to the continuous formation and breaking of chemical bonds, and the formation of chemical bonds will release an energy quantum, which is named "binding", and this energy may be large enough to excite electron–hole pairs.[40,45,55] Thus, even in the absence of strong frictional motion, "bindington" can occur under certain contact pressures. As shown in Fig. 1K and L, in the sliding mode, V_{oc} generated by the PBFD/PEDOT:PF interface increases from 0.27 V to 1.1 V, and the short-current density rises from 2.8 µA cm^{-2} to 19 µA cm^{-2} under mechanical pressures of 1–100 N. In the compression mode, V_{oc} increases from 0.2 V to 1.2 V, while the short-current density increases from 1.5 µA cm^{-2} to 15.7 µA cm^{-2}. In addition, the types of electrode materials for this back electrode were further investigated; typically, organic conducting carbon (OCC), metallic materials (Al, Ag, Au, Pt), and two-dimensional graphene(GR) were examined. As shown in Fig. S8 and S9 (ESI†), in both sliding and compression modes, except for the lower output performance of OCC compared to Ti$_3$C$_2$, the output performance of other electrode materials is close to Ti$_3$C$_2$.

8624 | *Energy Environ. Sci.*, 2024, **17**, 8621–8632

This journal is © The Royal Society of Chemistry 2024

Ti$_3$C$_2$ has great potential in the field of flexible electronics due to its high electrical conductivity, excellent mechanical properties and solution processability. We further compared the tensile-strain characteristics of semiconductor fibers at different electrodes. As shown in Fig. S10 (ESI†), PEDOT:PF@Ti$_3$C$_2$@CFs exhibits optimal tensile flexibility in P-type organic semiconductor fibers.

Based on the above DC output characteristics of the PBFD/PEDOT:PF interface, the electrical output of the single SF is further investigated. The influence of fiber diameter and excitation frequency on the electrical output of SFs in the compression and tensile states was investigated. As shown in Fig. 1M–P and Fig. S11 (ESI†), the V_{oc} and I_{sc} of SFs in the tensile state (30% strain) increased with increasing diameter and frequency, the V_{oc} is 0.18 V and I_{sc} is 1.5 μA at 0.2 mm, 1 Hz, and further increases to 1.29 V and 11.2 μA as the diameter increases to 10 mm and the frequency increases to 5 Hz. The tensile strain of these SFs and the electrical output at different strains were further investigated. As shown in Fig. S12 (ESI†), the maximum strain of SFs is about 87%, and the V_{oc} and I_{sc} increase from 0.37 V and 2.5 μA at 10% strain to 1.1 V and 9.3 μA at 80%. In the compression state, as shown in Fig. S13 (ESI†), the V_{oc} is 0.11 V and I_{sc} is 2 μA at 0.2 mm, 1 Hz, and further increases to 1.2 V and 11.1 μA as the diameter increases to 10 mm and the frequency increases to 5 Hz (It should be noted that, if not otherwise stated, 2 mm CFs were selected for this study).

Series/parallel characteristics and weaving design

At present, the fiber-based TVNGs face several challenges. The current designs utilize a metal-Al/fabric or fabric/fabric two-plane friction structure (Fig. 2A(i) and (ii)). However, this design is bulky, compromises clothing aesthetics, and is difficult to integrate into wearable electronic devices, thus limiting normal human activity. Furthermore, the existing TVNGs based on the Al/fabric or fabric/fabric interaction have limited output voltages (0.1–1.0 V) and currents (μA-level current) and can only harvest energy from one sliding direction. To enable a larger-scale application of fiber-based TVNGs on the human body, a three-dimensional TVNG with the following characteristics is required: high shape adaptability, excellent stability, high voltage (≥ 5 V), mA-level current, all-round energy harvesting, and easy integration (Fig. 2A(iii)). To fabricate this textile power source, as shown in Fig. 2B–D, analogous to a conventional battery structure, a single three-dimensional SF was assembled in series or parallel to investigate the V_{oc} and I_{sc} of the assembled textile. For the series connection of 1–50 sections of SFs, as shown in Fig. 2E and F, the V_{oc} of the textile increases from 0.45 to 24.5 V and the I_{sc} increases from 3.5 to 4.5 μA in the tensile state. As shown in Fig. 2G and H, the V_{oc} of the textile increases from 0.5 to 23 V, and the I_{sc} increases from 3.5 to 4.6 μA in the compression state. Similarly, in the case of a parallel connection of 1–50 sections of SF, as shown in Fig. 2I and J, the V_{oc} of the textile increases from 0.55 to 1.1 V and the I_{sc} increases from 4 to 176 μA in the stretched state. As shown in Fig. 2K and L, the V_{oc} of the textile increases from 0.58 to 0.88 V and the I_{sc} increases from 4.5 to 170 μA in the compression

state. In summary, as shown in Fig. S14 (ESI†), it can be concluded that series connection has a more pronounced effect on the V_{oc} of the assembled textile, and parallel connection has a more pronounced effect on the I_{sc} of the assembled textile, which is consistent with the series-parallel characteristics of commercially available batteries. Based on the series/parallel electrical properties of SFs, as shown in Fig. 2M and Fig. S15 (ESI†), in this study, 5 series SFs are used as a base assembly unit (5S-SF), and a 5S-SF × 5S-SF parallel structure is used as a sub-assembly unit (25SP-SF), and the SFs are woven into a wearable DC textile power source through a traditional weaving process and layer-by-layer assembly strategy (WDP). As shown in Fig. 2N(i)–(iv), the WDP has a double-layer structure that exhibits excellent flexibility and tensile properties.

More importantly, this dual-layer three-dimensional textile DC power source based on series/parallel combination mode has friction interfaces on the upper and lower surfaces of the textile and inside the textile compared to the plane/plane friction mode, which results in not only more friction contact sites, but also the ability to collect energy in three spatial directions, up and down, left and right, and front and back (Fig. S16, ESI†). For a wearable tribovoltaic power textile, the high voltage is more favorable for it to power a wide range of electronic devices, as shown in the figure below (Fig. S16, ESI†), compared to the friction of a single fiber in SFs; a single fiber in the 3D WDP has more friction contact sites, which will result in a higher V_{oc} and power output. On the other hand, the series mode in WDP with the double-layer structure further facilitates its V_{oc} increase.

In this study, the WDPs with areas of 5 × 10 cm^2, 10 × 10 cm^2, 10 × 20 cm^2 and 10 × 30 cm^2 are woven, and the V_{oc} and I_{sc} of WDPs under the low-frequency excitation of 1–5 Hz were further investigated. For quantitative characterization, a linear motor with a mechanical drive kit was used to simulate linear mechanical motion. Fig. 2O and P show that, under cyclic compression motion, as the frequency increases from 1 Hz to 5 Hz, for the 10 × 30 cm^2 WDPs, the V_{oc} increases from 10 to 40 V, and I_{sc} increases from 0.4 to 2.2 mA (Video S1 and S2, ESI†). Fig. 2Q and R show that, under cyclic tensile motion, as the frequency increases from 1 Hz to 5 Hz, the V_{oc} increases from 8 to 32 V, and I_{sc} increases from 0.45 to 1.8 mA (Detailed V_{oc} and I_{sc} for the other areas are recorded in Fig. S17 and S18, ESI†).

Electrical output and robustness of WDPs

Power density is an important metric for evaluating the WDPs. Herein, the 10 × 30 cm^2 WDPs were selected as the investigation object. As shown in Fig. 3A and C, the corresponding current magnitudes were obtained by externalizing different resistors, and the current in the loop decreases as the resistance increases. The output power density of the WDPs was further obtained by the formula: $P_d = I^2R/S$ (P_d is the power density, I is the current, R is the resistance and S is the fabric area). The maximum power density increased from 0.065 W m^{-2} at 1 Hz to 1.05 W m^{-2} at 5 Hz at a load resistance of about 35 kΩ in the compression state, and the maximum power density increased

This journal is © The Royal Society of Chemistry 2024

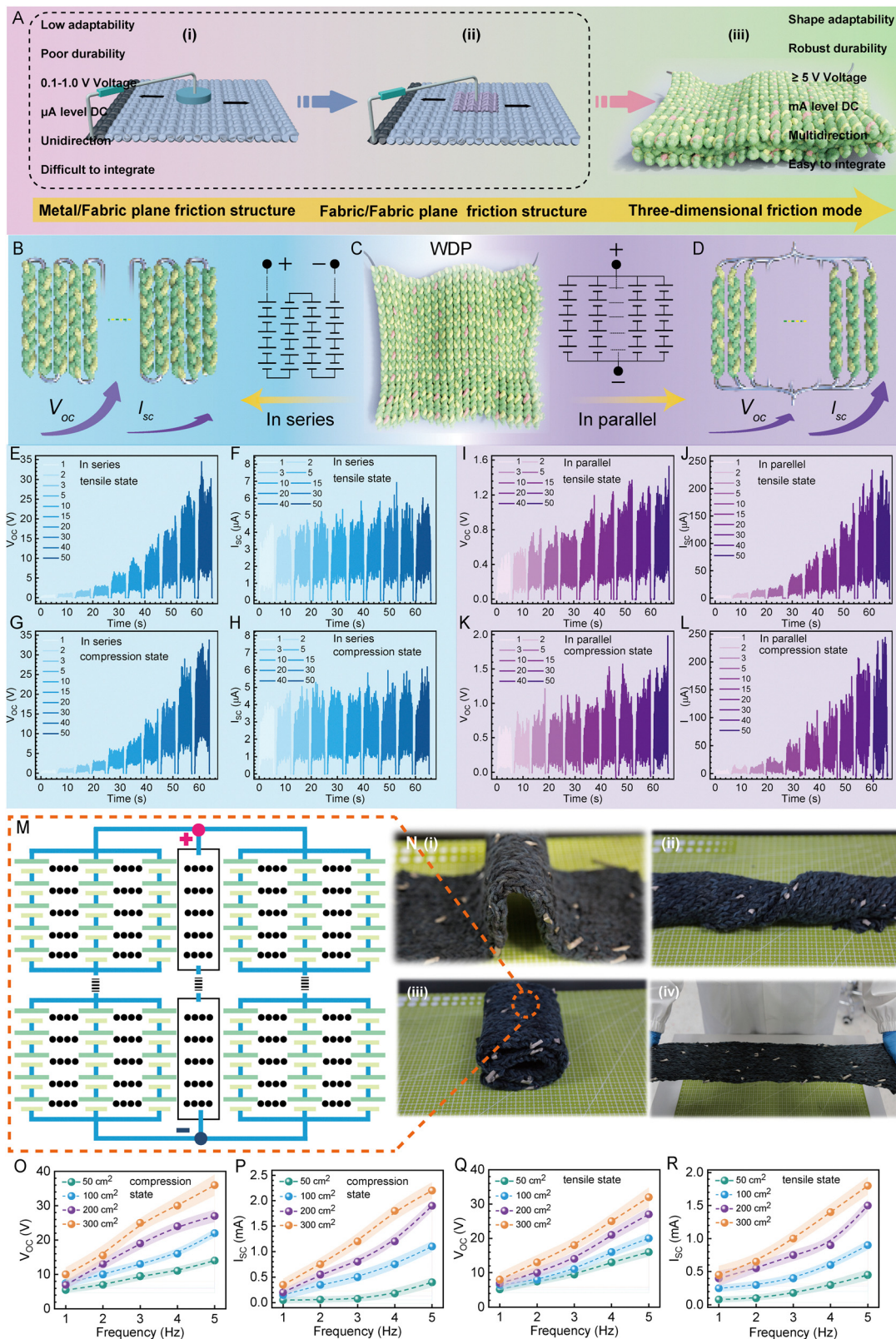Energy Environ. Sci., 2024, 17, 8621–8632 | 8625

Fig. 2 Series/parallel characteristics and weaving design. (A) Advantages of the 3D friction model compared with the plane friction model. (B)–(D) Schematic diagram of SFs series and parallel connections. (E)–(H) Electrical properties of SFs in series. (I)–(L) Electrical properties of SFs in parallel. (M) and (N) Design structure and optical photos of WDPs. (O)–(R) V_{OC} and I_{sc} of SFs under different areas and frequencies.
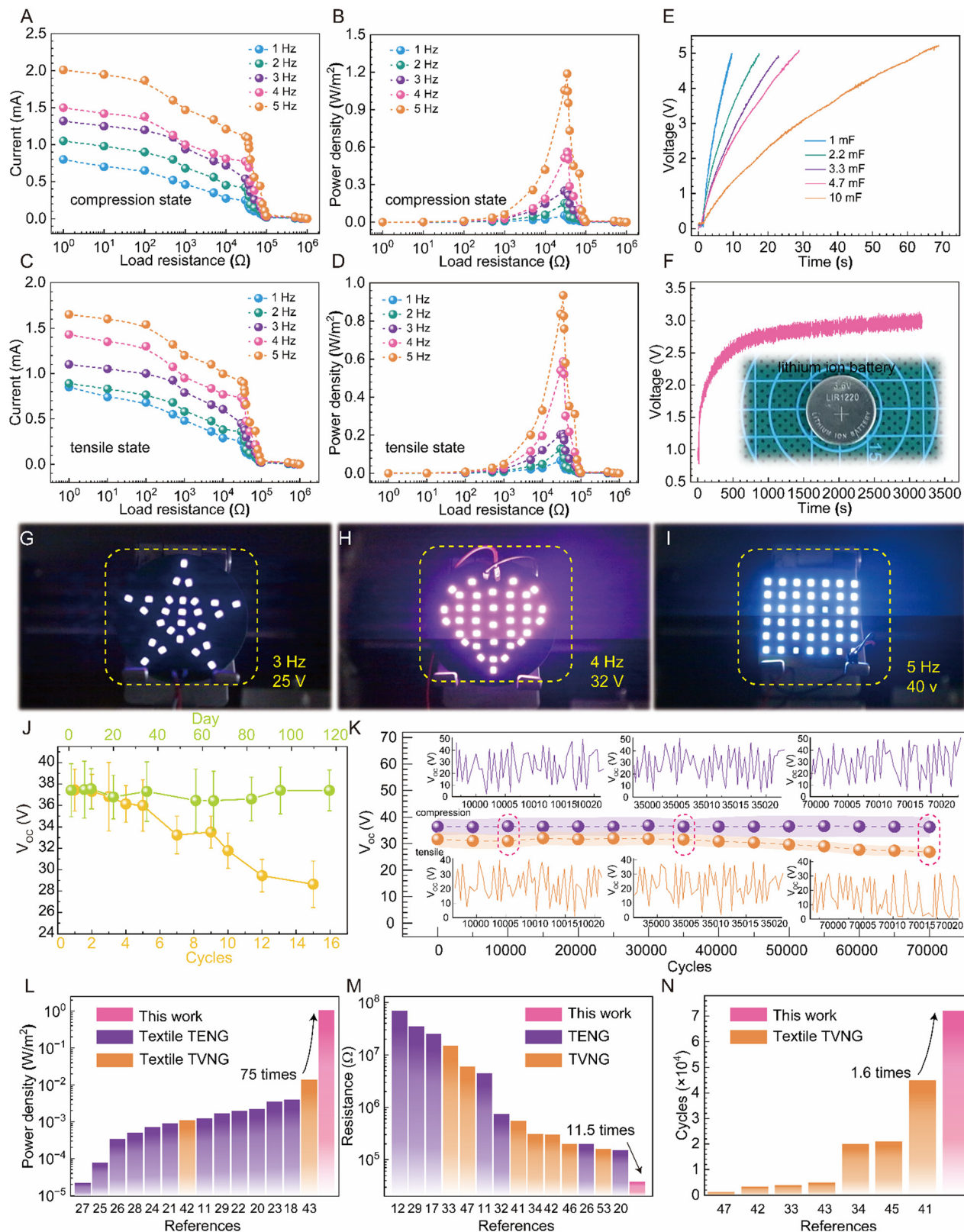
Fig. 3 Electrical output and durability. (A) and (B) Current and power density of WDPs at different frequencies in the compression state. (C) and (D) Current and power density of WDPs at different frequencies in the tensile state. (E) Charging characteristics of WDPs with 1, 2.2, 3.3, 4.7 and 10 mF capacitors. (F) Charging characteristics of WDP with a lithium-ion battery. (G)–(I) 25, 32 and 40 V colorful electric lamps were directly powered by WDPs at 3, 4 and 5 Hz, respectively. (J) Cycle washability and long-term durability of WDPs. (K) Durability test of the WDPs. (L)–(N) Comparison of power density, internal resistance and durability with the previous reports.

This journal is © The Royal Society of Chemistry 2024

Energy Environ. Sci., 2024, **17**, 8621–8632 | **8627**

Paper **Energy & Environmental Science**

from 0.08 W m^{-2} at 1 Hz to 0.96 W m^{-2} at 5 Hz at a load resistance of about 35 kΩ in the tensile state (Fig. 3B and D). Based on the high output power density of WDPs, as shown in Fig. 3E and F, where the capacitors or batteries were connected in series with the WDPs while a voltmeter was connected in parallel to detect the voltage of the devices. Capacitors of 1, 2.2, 3.3, 4.7 and 10 mF were continuously charged by the WDPs, and the capacitors of 1, 2.2, 3.3, 4.7 and 10 mF reached 5 V in 8.1, 17, 22.5, 28, and 67 s, respectively. We charged commercial energy storage devices such as capacitors and lithium-ion batteries at 5 Hz; more importantly, the power generated by the WDPs at 5 Hz could charge an 8 mAh commercial lithium-ion battery to 3.1 V in 55 minutes (Fig. 3F and Fig. S19, Video S3, ESI†). Due to the excellent morphological adaptability and wearability of WDP, it is worn on the body to obtain human movement energy to charge the battery. As shown in Fig. S20 (ESI†), it can charge the battery to 3.1 V in 102 minutes. The electricity generated by WDPs at 3, 4, and 5 Hz can also drive colorful electric lamps with working voltages of 25, 32, and 40 V, respectively (Fig. 3G–I and Video S4, ESI†), which provides a potential solution for them to drive high-voltage ($\geq$10 V) wearable electronic devices. As a sustainable textile power source, WDPs should have sufficient mechanical durability and chemical stability for practical applications, so the robustness of the textile was systematically investigated. First, the cyclic washability and long-term durability of WDP were investigated. As shown in Fig. 3J and Fig. S21 (ESI†), WDP maintained 70% of its output performance after 15 cycles of washing, and more importantly, the performance of WDP did

not deteriorate after 117 days. Furthermore, the electrical output of the WDPs gradually decreases to about 80% of its original value as the relative humidity increases from 5% to 90% (Fig. S22, ESI†). The increase in humidity will lead to an increase in water vapor in the environment, and a small amount of water vapor will adsorb on the surface of fibers, which will reduce the contact friction between fibers, thereby reducing the output performance of WDP. Distinguishing from the wear damage of the two planar friction modes, one of the advantages of the WDPs is the potential long-lasting durability, and to verify this advantage, the long-term output performance of the WDPs was tested in compression and tensile motion modes as shown in Fig. 3K and Fig. S23 (ESI†). Obviously, the WDPs have excellent durability, and their voltage did not drop significantly after 72 000 cycles. The WDPs were compared with the previously reported TENGs and TVNGs, which achieved a 75-fold increase in power density, 11.5-fold decrease in internal resistance, and 1.6-fold increase in durability (Fig. 3L–N, the detailed numerical parameters are recorded in Table 1).

Prospects and applications of WDPs

Benefiting from the characteristics of high DC, excellent morphological adaptability, low internal resistance and environmental stability of WDPs, as shown in Fig. 4A, they have a great potential for harvesting biomechanical energy from the human body to continuously power wearable electronic devices. As shown in Fig. 4B–D, the WDPs were fixed on the elbow, knee, and feet of the human body, and they matched the movement of the human body shape. The WDPs generate V_{oc}

Table 1 The performance of different types TVNGs and TENGs

| Material	TVNG/ TENG	DC/AC	Textile	Hydrophobic	Flexibility	Stretchability	V_{oc} (V)	Power density (W m^{-2})	Resistance (MΩ)	Durability (Cycles)	Ref.
Cu/PTFE	TENG	AC	✓	✗	✓	✗	6	1.25×10^{-3}	10	—	11
CNT/PTFE	TENG	AC	✓	✗	✓	✗	20	4×10^{-3}	1000	10 000	18
Ag/PTFE	TENG	AC	✓	✗	✓	✗	900	2×10^{-3}	100	—	22
Water/PTFE	TENG	AC	✗	✓	✗	✗	150	50.1	0.3	—	32
Ag/PDMS	TENG	AC	✓	✗	✓	✓	48	—	2000	—	12
Graphene/PDMS	TENG	AC	✓	✗	✓	✗	70	30×10^{-3}	100	—	23
PE/PDMS	TENG	AC	✓	✓	✓	✓	200	0.8×10^{-3}	1000	5700	21
Ag/PDMS	TENG	AC	✓	✗	✓	✓	20	22×10^{-6}	150	1800	27
Conductive yarn/PI	TENG	AC	✓	✓	✓	✓	140	70×10^{-6}	1000	—	25
Conductive polyamide/PI	TENG	AC	✓	✓	✓	✓	0.12	0.12	10	1000	29
Bi$_2$Te$_3$/Kapton	TENG	AC	✗	✗	✗	✗	50	—	30	—	17
Ag/PE	TENG	AC	✓	✗	✗	✓	40	10.5×10^{-3}	1000	10 000	28
Ag/Nylon	TENG	AC	✓	✗	✓	✓	20	2.2×10^{-3}	20	10 000	20
Ag/EP	TENG	AC	✓	✗	✗	✓	18	0.7	24	—	24
Conductive yarn/PAN:PVDF	TENG	AC	✓	✓	✓		30	350×10^{-6}	500	—	26
n-SWCNT/ p-SWCNT	TVNG	DC	✓	✗	✗	✗	0.3	—	3.3	1280	47
GaN/Bi$_2$Te$_3$	TVNG	DC	✗	✗	✗	✗	130	11.85	0.16	—	53
MoS$_2$/Ta$_4$C$_3$	TVNG	DC	✓	✗	✓	✗	0.3	37×10^{-3}	0.55	54 000	41
Al/PEDOT:PSS	TVNG	DC	✓	✗	✓	✗	0.6	—	—	4000	33
Al/PEDOT:PSS	TVNG	DC	✗	✗	✓	✗	2	—	0.2	20 000	34
Al/PEDOT:PSS	TVNG	DC	✓	✗	✓	✗	0.45	1.2×10^{-3}	30	3350	42
Al/PEDOT:PSS	TVNG	DC	✓	✗	✓	✗	0.8	0.13	0.01	5000	43
Al/PPy	TVNG	DC	✓	✗	✓	✗	0.4	0.17	0.43	20 000	45
Au/PPy	TVNG	DC	✗	✗	✓	✗	0.7	0.15	0.0082	—	46
PBFD/PEDOT:PF	TVNG	DC	✓	✓	✓	✓	40	1.05	0.035	72 000	This work
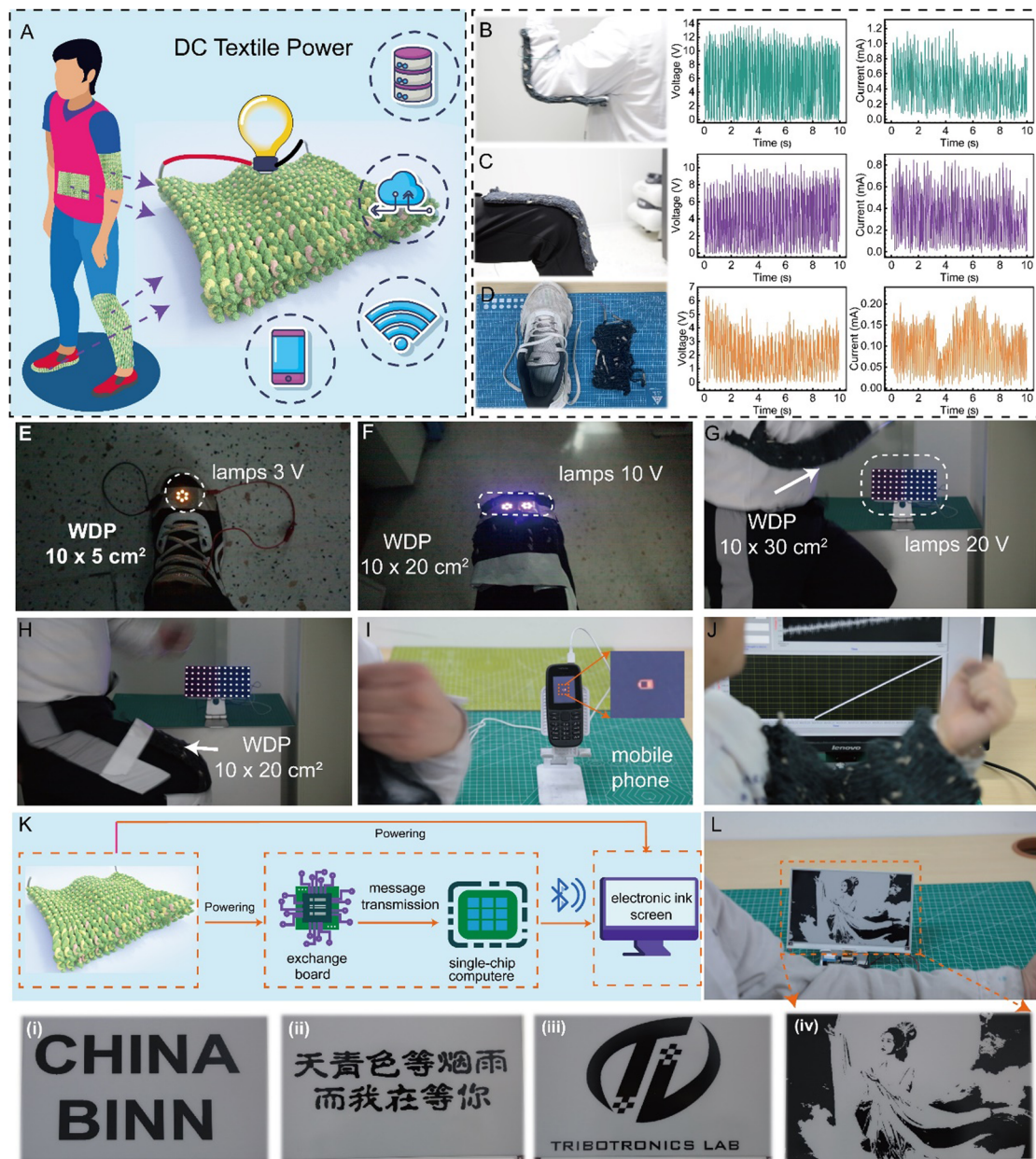
Fig. 4 Application and Prospect Demonstration. (A) The outlook of WDPs in wearable electronics filed by harvesting biokinetic energies. (B)–(D) Demonstration of the WDPs for harvesting biomechanical energy from different parts of the human body. (E)–(H) Demonstration of driving 3, 10 and 20 V lamps by harvesting biokinetic energies. (I) Demonstration of directly charging a mobile phone. (J) Demonstration of directly charging a 1 mF capacitor. (K) and (L) Demonstration of directly powering a 1 mF capacitor, a bluetooth circuit and the 16×10 cm^2 e-ink screens system.

of 10, 7, 2.5 V and I_{sc} of 0.6, 0.5 and 0.14 mA on the elbow, knee, and feet of the human body, respectively. Furthermore, the colored lights with 3, 10 and 20 V working voltages are continuously powered by the WDPs by harvesting human biomechanical energy, and due to the relatively high V_{oc} of the WDPs, the bright light of the colored lights can be observed even in non-dark environments (Fig. 4E–H and Video S5, ESI†). Surprisingly, under human biomechanical motion, WDPs can directly power a 25 mW commercial mobile phone, a 10 mW smart bracelet, and a 8 mW thermo-hygrometer without any power management circuitry (Fig. 4I and Fig. S24, Video S6, ESI†),

and the power delivered from the WDPs is also capable of charging a 1 mF commercial capacitor up to 3.0 V with about 95 s in at fast bending speeds (Fig. 4J and Fig. S25, Video S7, ESI†). The effect of charging the capacitor at different bending speeds was further investigated, as can be seen in Fig. S25 (ESI†), 82 s to 3.0 V at faster bending speeds, 110 s to 3.0 V at normal bending speeds, and 175 s to 3.0 V at slower bending speeds. To further evaluate the role of WDPs as a flexible power source in the field of self-powered motion monitoring systems, we designed a human motion detection system (HMDS). As shown in Fig. S26A and B (ESI†), when humans walk, the voltage generated by the WDP in

This journal is © The Royal Society of Chemistry 2024

Energy Environ. Sci., 2024, **17**, 8621–8632 | **8629**

the sole part of the shoe is 3.5 V, and the LED of the system will not light up. When humans run, the voltage generated by the WDP in the sole is 7 V, and the LED of the system starts to light up. In particular, the WDP is used for powering a Bluetooth ink screen display system (BIS); Fig. 4K indicates the circuit diagram of the BIS, which consists of circuit management, a storage capacitor, a bluetooth transmitting system (Fig. S27, ESI†) and a 16×10 cm^2 ink electronic screen. The WDPs can continuously power both the system circuitry and ink electronic screen; as a result, the BIS system can transfer English phrases, Chinese characters, ICONS and complex human body images from the bluetooth transmitting system to the e-ink screen (Fig. 4L and Video S8, ESI†). Finally, the effect of the human skin and clothing on the performance of WDPs was investigated. The WDPs were worn on human skin and on a variety of clothing materials. As shown in Fig. S28 (ESI†), the performance of WDP textiles on a down coat is slightly higher than that on other garments, such as skin and shirts, due to the fact that the elasticity of the down coat is more sensitive to forces due to the other garments, and the performance of WDP textiles in noise is also slightly higher than that in quiet environments due to the tiny vibrations caused by the environment.

Conclusions

In summary, we report a high-performance, truly wearable tribovoltaic DC power supply textile based on the P/N-type organic semiconductor weaving and series/parallel layer-by-layer assembly strategy. First, the single P/N-type semiconductor fibers were helically wound to obtain a 3D SF with tighter interfacial friction. Subsequently, a power textile (WDP) with morphological adaptability, mechanical flexibility and moisture resistance was manufactured by a traditional weaving process. The WDP is a two-layer interlocking structure, which is highly deformable and can be manufactured in controlled sizes. Benefiting from the series/parallel layer-by-layer assembly strategy, it achieves an output power density of about 1.05 W m^{-2} and a V_{oc} of 40 V. Compared to reported studies, the WDPs have high flexibility, excellent environmental robustness (72 000 cycles), lower internal resistance, high voltage and it still maintains 80% output performance in an environment with 90% humidity. The WDPs still maintain 70% output performance after being washed 15 times and 117 days. The WDPs achieve a 11.5-fold reduction in internal resistance and a 1.6-fold increase in durability compared to previous textile TENGs and TVNGs. For a wearable textile device, the WDPs achieve an 8-fold increase in V_{oc} compared to previous textile TVNGs. The WDPs can charge a 10 mF commercial capacitor to 5 V in 67 s and a commercial lithium-ion battery to 3 V in 55 min and the DC generated by WDPs from the human body is enough to power lamps with 3, 12 and 20 V working voltage. The wearable WDPs are well adapted to the biomechanical movements of the human body and are easy to integrate into wearable and portable electronics; this textile can generate enough electricity for various practical applications, including light-colored lights with different voltages, continuously driving mobile phones, smart electronic

meters, temperature and humidity meters, and supplying power to Bluetooth transmission systems and 16×10 cm^2 ink electronic screens. This hybrid textile can be widely used not only in self-powered electronics but also for larger-scale DC power generation. The high-performance WDPs demonstrated in this work provide a promising strategy for the practical application of the tribovoltaic effect in the field of textile power supplies and smart wearable electronics.

Methods

Fabrication of PEDOT:PF

PEDOT:PF was synthesized *via* oxidation chemical polymerization. First, 10 mL of aqueous PF ionomer dispersion and 0.1 g of PEDOT were mixed in 20 mL of deionized water, followed by vigorous stirring for 2 h to form an emulsion. Then, 0.2 g FeCl$_3$ was added as an oxidizing agent, and after continuous stirring at 20 °C for 24 h, the obtained polymer dispersion was purified with a semi-permeable membrane, and the residual oxidizing agent and PEDOT were removed. After purification, the dark blue aqueous dispersion was then centrifuged. The resulting product was dispersed in ethanol. By adjusting the molar ratio of PEDOT to PF ionomer, PEDOT:PF with different molar ratios were obtained.

Fabrication of Ti$_3$C$_2$, Ti$_3$C$_2$@CFs and PEDOT:PF@Ti$_3$C$_2$@CFs

The Ti$_3$AlC$_2$ powder was immersed in a 50% HF solution and stirred at 25 °C for 24 h. Then, the resulting multilayer Ti$_3$C$_2$ nanosheets were obtained by centrifuging and ultrasonicating the HF-etched Ti$_3$C$_2$ nanosheets. Cotton fibers (CFs) were plasma treated for 10 min in an O$_2$ atmosphere; then, the fibers were ultrasonically modified in 1.0 mg mL^{-1} cetyltrimethylammonium bromide (CTAB) solution for 15 min to obtain CF-CTAB composite fibers. Finally, the CF-CTAB was immersed in the prepared 5 mg mL^{-1} multilayer Ti$_3$C$_2$ solution for 2 h and then vacuum dried at 60 °C for 12 h to obtain Ti$_3$C$_2$@CF composite fibers. Ti$_3$C$_2$@CF was immersed in a PEDOT:PF solution for 4 h (1 cm of PEDOT:PF@Ti$_3$C$_2$ was reserved as the electrode interface) and subsequently vacuum-dried at 60 °C for 12 h to obtain PEDOT:PF@Ti$_3$C$_2$@CF semiconductor fibers.

Fabrication of PBFD and PBFD @CFs

PBFD solutions were prepared using the reported methods. Briefly, PBFDs were obtained by oxidative polymerisation and *in situ* reductive doping processes in the presence of a quinone oxidising agent using 3,7-dihydrobenzo [1,2-*b*:4,5-*b′*] difuran-2,6-dione as the precursor. Different quinones, including ubiquinone and idebenone, were employed to obtain PBFD solutions. For the preparation of PBFD@CFs semiconductor fibers, the CFs were first plasma-treated for 5 min in an O$_2$ atmosphere, and then the CFs were further immersed in the PBFD solution with continuous stirring at 60 °C for 2 h, and then vacuum-dried at 50 °C for 24 h to obtain PBFD@CF semiconductor fibers.

8630 | *Energy Environ. Sci.*, 2024, **17**, 8621–8632

This journal is © The Royal Society of Chemistry 2024

Weaving strategy for the WDPs

For the preparation of SF, as shown in Fig. S3 (ESI†), a 40 cm of PEDOT:PF@Ti$_3$C$_2$@CFs was first bent and folded in half, and the bend was fixed and knotted with one end of a 20 cm of PBFD@CF (1 cm of the knotted end of the PBFD@CF was reserved for the interface of the electrode). Subsequently, the knotted end was fixed to a textile support, the three fibers at the open end were helically wound, and finally, the open end of the fiber helix was knotted to form the SF (1 cm of the open end of the PEDOT:PF@Ti$_3$C$_2$@CFs was reserved as the interface of the electrode). The 5S-SF was fabricated by sequentially connecting the positive and negative electrode interfaces reserved in the SF. For the preparation of the WDP, the positive electrode of the 1st 5S-SFs was firstly fixed with the middle of the 1, 2 pillars of the elliptical bracket, followed by winding the 5S-SFs along the path of the outer ends of the 1, 3, 5, 7 pillars, further winding the 5S-SFs along the path of the outer ends of the 8, 6, 4, 2 pillars, and finally reserving the negative electrode of the 5S-SFs at the outer ends of the pillars. The positive electrode of the 2nd 5S-SFs is fixed with the middle of the 7, 8 pillars of the elliptical support, and the winding process is reversed from the path of the first one, and finally, the fibers of the 1st one at the outer end of the 1, 3, 5, 7 and 2, 4, 6, 8 pillars are turned away from the top to the inner end to hold down the 2nd 5S-SFs. The same process is repeated in this way with the subsequent odd-numbered 5S-SFs and the even-numbered 5S-SFs, in order to prepare the double-layer WDPs.

Characterization

Plasma treatment was carried out by a SUNJUNE PLASMA VP-R5 in an O$_2$ atmosphere. Samples were characterized utilizing X-ray diffraction (XRD, Cu Kα, λ = 0.154 nm, 40 kv, 40 mA). Work functions of samples were measured by KPFM (Bruker Dimension FastScan Multimode8). The *I–V* curve was measured by a Keithley 2612b. Electrical performance was measured by a low-noise electrometer (Keithley 6514, USA). The surface morphology of the samples was characterized by a field emission scanning electron microscope (SEM, SU8020, Hitachi, Japanese).

DFT

The geometry of all molecules was optimized by density functional theory (DFT). All the DFT computations were performed using the M06-2X density functional method. The def2-SVP basis set was used for geometry optimization. All structures were generated using CYLview. All these calculations were performed with the Gaussian 16 software package, and the molecular distance between PBFD and PEDOT:PF was 2.48 angstroms.

Author contributions

Conceptualization: BBF, methodology: BBF, CZ, RFL, investigation: BBF, ZFD, YMD, visualization: BBF, GXL, RFL, LKG, supervision: GXL, CZ, writing – original draft: BBF, CZ, ZLW, writing – review & editing: CZ, ZLW, software: BBF, LKG, ZZ, editing: BBF, LKG. All the authors discussed the results and commented on the manuscript.

Data availability

The experimental methods of this manuscript have been described in detail in Methods. The PDEOT and PBFD-related references described in this manuscript are 48 and 52. The data supporting this article have been included as part of the ESI.†

Conflicts of interest

The authors declare no competing financial interest.

Acknowledgements

Notes and references

1 X. Zhao, H. Askari and J. Chen, *Joule*, 2021, **5**, 1391–1431.

2 Q. Zhang, C. Xin, F. Shen, Y. Gong, Y. Zi, H. Guo, Z. Li, Y. Peng, Q. Zhang and Z. L. Wang, *Energy Environ. Sci.*, 2022, **15**, 3688–3721.

3 Q. Shi, B. Dong, T. He, Z. Sun, J. Zhu, Z. Zhang and C. Lee, *InfoMat*, 2020, **2**, 1131–1162.

4 R. Liu, Z. L. Wang, K. Fukuda and T. Someya, *Nat. Rev. Mater.*, 2022, **7**, 870–886.

5 J. Wang, S. Li, F. Yi, Y. Zi, J. Lin, X. Wang, Y. Xu and Z. L. Wang, *Nat. Commun.*, 2016, **7**, 12744.

6 S. Zhang, M. Chi, J. Mo, T. Liu, Y. Liu, Q. Fu, J. Wang, B. Luo, Y. Qin, S. Wang and S. Nie, *Nat. Commun.*, 2022, **13**, 4168.

7 A. J. Bandodkar, S. P. Lee, I. Huang, W. Li, S. Wang, C.-J. Su, W. J. Jeang, T. Hang, S. Mehta, N. Nyberg, P. Gutruf, J. Choi, J. Koo, J. T. Reeder, R. Tseng, R. Ghaffari and J. A. Rogers, *Nat. Electron.*, 2020, **3**, 554–562.

8 B. Dunn, H. Kamath and J.-M. Tarascon, *Science*, 1979, **334**, 928–935.

9 L. Yin, J.-M. Moon, J. R. Sempionatto, M. Lin, M. Cao, A. Trifonov, F. Zhang, Z. Lou, J.-M. Jeong, S.-J. Lee, S. Xu and J. Wang, *Joule*, 2021, **5**, 1888–1904.

10 G. Chen, Y. Li, M. Bick and J. Chen, *Chem. Rev.*, 2020, **120**, 3668–3720.

11 J. Chen, Y. Huang, N. Zhang, H. Zou, R. Liu, C. Tao, X. Fan and Z. L. Wang, *Nat. Energy*, 2016, **1**, 16138.

12 K. Dong, X. Peng, J. An, A. C. Wang, J. Luo, B. Sun, J. Wang and Z. L. Wang, *Nat. Commun.*, 2020, **11**, 2868.

13 A. Libanori, G. Chen, X. Zhao, Y. Zhou and J. Chen, *Nat. Electron.*, 2022, **5**, 142–156.

14 H. H. Shi, Y. Pan, L. Xu, X. Feng, W. Wang, P. Potluri, L. Hu, T. Hasan and Y. Y. S. Huang, *Nat. Mater.*, 2023, **22**, 1294–1303.

This journal is © The Royal Society of Chemistry 2024

Energy Environ. Sci., 2024, **17**, 8621–8632 | **8631**

15 Y. Jing, J. Luo, X. Han, J. Yang, Q. Liu, Y. Zheng, X. Chen, F. Huang, J. Chen, Q. Zhuang, Y. Shen, H. Chen, H. Zhao, G. J. Snyder, G. Li, T. Zhang and K. Zhang, *Energy Environ. Sci.*, 2023, **16**, 4334–4344.

16 S. J. Kim, J. H. We and B. J. Cho, *Energy Environ. Sci.*, 2014, **7**, 1959.

17 M. Li, H.-W. Lu, S.-W. Wang, R.-P. Li, J.-Y. Chen, W.-S. Chuang, F.-S. Yang, Y.-F. Lin, C.-Y. Chen and Y.-C. Lai, *Nat. Commun.*, 2022, **13**, 938.

18 J. Yi, K. Dong, S. Shen, Y. Jiang, X. Peng, C. Ye and Z. L. Wang, *Nano-Micro Lett.*, 2021, **13**, 103.

19 H. Zhang, Z. Wang, H. Li, M. Salla, Y. Song, S. Huang, S. Huang, X. Wang, K. Liu, G. Xu, J. Huang, C.-W. Qiu and Q. Wang, *Joule*, 2023, **7**, 1515–1528.

20 M. Zhou, F. Xu, L. Ma, Q. Luo, W. Ma, R. Wang, C. Lan, X. Pu and X. Qin, *Nano Energy*, 2022, **104**, 107885.

21 M. Cheng, X. Liu, Z. Li, Y. Zhao, X. Miao, H. Yang, T. Jiang, A. Yu and J. Zhai, *Chem. Eng. J.*, 2023, **468**, 143800.

22 R. Cheng, C. Ning, P. Chen, F. Sheng, C. Wei, Y. Zhang, X. Peng, K. Dong and Z. L. Wang, *Adv. Energy Mater.*, 2022, 01532.

23 I. Domingos, Z. Saadi, K. S. Sadanandan, H. A. Pocinho, D. M. Caetano, A. I. S. Neves, M. F. Craciun and H. Alves, *Nano Energy*, 2023, **115**, 108688.

24 J. Huang, S. Wang, X. Zhao, W. Zhang, Z. Chen, R. Liu, P. Li, H. Li and C. Gui, *Mater. Horiz.*, 2023, **10**, 3840–3853.

25 L. Ma, R. Wu, S. Liu, A. Patil, H. Gong, J. Yi, F. Sheng, Y. Zhang, J. Wang, J. Wang, W. Guo and Z. L. Wang, *Adv. Mater.*, 2020, 03897.

26 L. Ma, M. Zhou, R. Wu, A. Patil, H. Gong, S. Zhu, T. Wang, Y. Zhang, S. Shen, K. Dong, L. Yang, J. Wang, W. Guo and Z. L. Wang, *ACS Nano*, 2020, **14**, 4716–4726.

27 C. Ning, K. Dong, R. Cheng, J. Yi, C. Ye, X. Peng, F. Sheng, Y. Jiang and Z. L. Wang, *Adv. Funct. Mater.*, 2020, 06679.

28 C. Wei, R. Cheng, C. Ning, X. Wei, X. Peng, T. Lv, F. Sheng, K. Dong and Z. L. Wang, *Adv. Funct. Mater.*, 2023, 03562.

29 R. Wu, S. Liu, Z. Lin, S. Zhu, L. Ma and Z. L. Wang, *Adv. Energy Mater.*, 2022, 01288.

30 B. Fan, G. Liu, X. Fu, Z. Wang, Z. Zhang and C. Zhang, *Chem. Eng. J.*, 2022, **446**, 137263.

31 F.-R. Fan, Z.-Q. Tian and Z. Lin Wang, *Nano Energy*, 2012, **1**, 328–334.

32 W. Xu, H. Zheng, Y. Liu, X. Zhou, C. Zhang, Y. Song, X. Deng, M. Leung, Z. Yang, R. X. Xu, Z. L. Wang, X. C. Zeng and Z. Wang, *Nature*, 2020, **578**, 392–396.

33 P. Deng, Y. Wang, R. Yang, Z. He, Y. Tan, Z. Chen, J. Liu and T. Li, *Adv. Sci.*, 2022, 07298.

34 F. Jiang, G. Thangavel, X. Zhou, G. Adit, H. Fu, J. Lv, L. Zhan, Y. Zhang and P. S. Lee, *Adv. Mater.*, 2023, 02815.

35 G. Liu, R. Luan, Y. Qi, L. Gong, J. Cao, Z. Wang, F. Liu, J. Zeng, X. Huang, Y. Qin, S. Dong, Y. Feng, L.-B. Huang and C. Zhang, *Nano Energy*, 2023, **106**, 108075.

36 Z. L. Wang and A. C. Wang, *Mater. Today*, 2019, **30**, 34–51.

37 Z. Zhang, D. Jiang, J. Zhao, G. Liu, T. Bu, C. Zhang and Z. L. Wang, *Adv. Energy Mater.*, 2019, 03713.

38 M. Zheng, S. Lin, L. Xu, L. Zhu and Z. L. Wang, *Adv. Mater.*, 2020, 00928.

39 J. Liu, A. Goswami, K. Jiang, F. Khan, S. Kim, R. McGee, Z. Li, Z. Hu, J. Lee and T. Thundat, *Nat. Nanotechnol.*, 2018, **13**, 112–116.

40 S. Lin and Z. Lin Wang, *Mater. Today*, 2023, **62**, 111–128.

41 B. Fan, Z. Wang, G. Liu, Z. Wang, X. Fu, L. Gong and C. Zhang, *Adv. Funct. Mater.*, 2023, 01821.

42 J. Meng, Z. H. Guo, C. Pan, L. Wang, C. Chang, L. Li, X. Pu and Z. L. Wang, *ACS Energy Lett.*, 2021, **6**, 2442–2450.

43 R. Yang, M. Benner, Z. Guo, C. Zhou and J. Liu, *Adv. Function Mater.*, 2021, 03132.

44 X. Ding, H. Shao, H. Wang, R. Bai, J. Fang and T. Lin, *J. Mater. Chem. A*, 2022, **10**, 13055–13065.

45 J. Meng, C. Pan, L. Li, Z. H. Guo, F. Xu, L. Jia, Z. L. Wang and X. Pu, *Energy Environ. Sci.*, 2022, **15**, 5159–5167.

46 H. Shao, J. Fang, H. Wang, L. Dai and T. Lin, *Adv. Mater.*, 2016, **28**, 1461–1466.

47 T. Lv, R. Cheng, C. Wei, E. Su, T. Jiang, F. Sheng, X. Peng, K. Dong and Z. L. Wang, *Adv. Energy Mater.*, 2023, 01178.

48 Y. Jiang, X. Dong, L. Sun, T. Liu, F. Qin, C. Xie, P. Jiang, L. Hu, X. Lu, X. Zhou, W. Meng, N. Li, C. J. Brabec and Y. Zhou, *Nat. Energy*, 2022, **7**, 352–359.

49 T. J. Cuthbert, B. C. Hannigan, P. Roberjot, A. V. Shokurov and C. Menon, *Adv. Mater.*, 2022, 09321.

50 C. Ning, R. Cheng, Y. Jiang, F. Sheng, J. Yi, S. Shen, Y. Zhang, X. Peng, K. Dong and Z. L. Wang, *ACS Nano*, 2022, **16**, 2811–2821.

51 L. Wang, F. Wan, Y. Xu, S. Xie, T. Zhao, F. Zhang, H. Yang, J. Zhu, J. Gao, X. Shi, C. Wang, L. Lu, Y. Yang, X. Yu, S. Chen, X. Sun, J. Ding, P. Chen, C. Ding, F. Xu, H. Yu and H. Peng, *Nat. Nanotechnol.*, 2023, **18**, 1085–1093.

52 H. Tang, Y. Liang, C. Liu, Z. Hu, Y. Deng, H. Guo, Z. Yu, A. Song, H. Zhao, D. Zhao, Y. Zhang, X. Guo, J. Pei, Y. Ma, Y. Cao and F. Huang, *Nature*, 2022, **611**, 271–277.

53 Z. Zhang, Z. Wang, Y. Chen, Y. Feng, S. Dong, H. Zhou, Z. L. Wang and C. Zhang, *Adv. Mater.*, 2022, 00146.

54 M. K. Beyer and H. Clausen-Schaumann, *Chem. Rev.*, 2005, **105**, 2921–2948.

55 Y. Lu, Y. Yan, X. Yu, X. Zhou, S. Feng, C. Xu, H. Zheng, Z. Yang, L. Li, K. Liu and S. Lin, *Research*, 2021, 7505638.

8632 | *Energy Environ. Sci.*, 2024, **17**, 8621–8632

This journal is © The Royal Society of Chemistry 2024